J. Fluid Mech. (2026), *vol.* 1036, A1, doi:10.1017/jfm.2026.11565

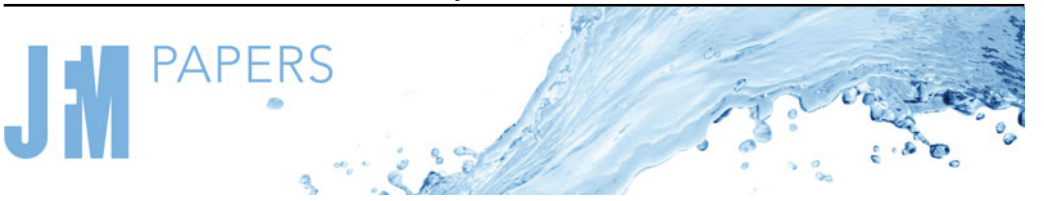

Influence of Reynolds number on the pressure gradient of turbulent channel flow with heterogeneous roughness

Carola Schmidt[1], **Patricia Sujar-Garrido**[1,2], **Ute Schmitgen**[1] **and Bettina Frohnapfel**[1]

[1]Institute of Fluid Mechanics, Karlsruhe Institute of Technology, Karlsruhe, Germany

[2]Department of Engineering Mechanics, KTH Royal Institute of Technology, Stockholm, Sweden

Corresponding author: Bettina Frohnapfel, bettina.frohnapfel@kit.edu

(Received 12 May 2025; revised 31 March 2026; accepted 8 April 2026)

Pressure-gradient measurements are reported for turbulent channel flows over six heterogeneous rough surfaces with 50 % roughness coverage, composed of P60 sandpaper patches arranged as streamwise-aligned strips, spanwise-aligned strips, or a checkerboard pattern of square patches. A new metric quantifies the relative pressure-gradient increase of heterogeneous surfaces compared with a homogeneous rough (100 % roughness coverage) surface. Above a surface-dependent critical Reynolds number, this metric $\Delta\Pi^*$ becomes almost independent of Re_b for all investigated surfaces, whereas below this threshold a clear dependence is observed. Complementary hot-wire measurements provide insight into the corresponding flow fields. According to the flow field data, the surfaces exhibiting the smallest $\Delta\Pi^*$ at low Re_b appear almost homogeneous to the flow, a feature that is not present at higher Reynolds number. Based on these observations the concept of a hydraulically heterogeneous surface is introduced. Surfaces with sandpaper patch dimensions of the order of the channel half-height can be perceived by the flow as homogeneous when the Reynolds number is low. As Re_b rises, surface heterogeneity translates into flow heterogeneity, which first intensifies in the transitionally heterogeneous regime, then approaches an almost self-similar state in the fully heterogeneous regime where $\Delta\Pi^*$ is approximately constant. In this regime, comparable pressure gradients for surfaces that generate markedly different mean flow fields indicate that turbulent secondary flows induced by streamwise-aligned roughness strips have little effect on

overall drag. Remarkably, the pressure gradient in this regime is captured well by a simple predictive model.

Key words: turbulent flows, turbulent boundary layers

1. Introduction

The available predictive tools for the flow resistance of rough surfaces were designed for surfaces in which random roughness is homogeneously distributed in a statistical sense. While this is a reasonable assumption for many real-world scenarios, other flow scenarios include heterogeneous rough surfaces, and at present we do not know how to include the statistically heterogeneous character of such surfaces in predictive drag models (Chung *et al.* 2021).

For surfaces consisting of large patches (i.e. larger than the outer scale δ of the flow) with constant roughness properties within each patch, the idea was developed to build a prediction of the global drag based on the drag behaviour of the corresponding subsurfaces (Bou-Zeid *et al.* 2020; Neuhauser *et al.* 2022; Hutchins *et al.* 2023). These approaches rely on the assumption that the individual patches are large enough for the turbulent flow to be in local equilibrium with the surface, and edge effects are negligible. While the impact of a homogeneous rough surface on turbulent flow can be characterised by a single quantity that is valid for external boundary layers and internal duct flows (e.g. a roughness function or an equivalent sand grain roughness height), the existing predictive suggestions for the global drag of heterogeneous rough (patchy) surfaces additionally build on the particular physics of the canonical flow configurations; i.e. they consider either external boundary layers or internal (channel) flows. In addition, the introduction of large length scales in the surface pattern can impact the flow beyond the classical roughness sublayer such that deviations from the equilibrium state might not be identical in external and internal flow configurations. It is thus most likely not straightforward to transfer results for the global drag of heterogeneous rough surfaces from internal flows to external ones, and vice versa. The present work concerns internal flows.

Two canonical classes of heterogeneous rough surfaces have been studied rather intensively in the literature. These are smooth–rough transitions in either the spanwise or streamwise flow direction. Streamwise-aligned roughness strips (often termed strip-type roughness) belong to the former group, and the primary interest of most studies concerns the induced turbulent secondary motion over such surfaces. The corresponding studies were carried out either in turbulent boundary layers (e.g. Anderson *et al.* 2015; Wangsawijaya *et al.* 2020) or in channel flows (e.g. Hinze 1973; Frohnapfel *et al.* 2024). For such strip-type roughness, drag predictions based on a local equilibrium assumption show good agreement with low Reynolds number direct numerical simulations (DNS) data in turbulent channel flow for a variety of strip widths, with only slightly increased drag coefficients in configurations with pronounced turbulent secondary motions (Neuhauser *et al.* 2022). However, significant deviations of the prediction with measurement data were found over streamwise-aligned sandpaper strips (P60 grit sandpaper of widths δ and 2δ, with δ being the channel half-height) for higher Reynolds numbers (Frohnapfel *et al.* 2024). Possible explanations for this deviation include, in addition to the presence of turbulent secondary motions, the impact of spanwise transients in the flow rate distribution (Neuhauser *et al.* 2025). The assumption of local equilibrium

was thus found not to be a good assumption for these (spanwise heterogeneous) strip-type surfaces, which is not surprising due to limited strip width.

The numerical studies of Chung, Monty & Hutchins (2018) and Andreolli *et al.* (2025) in turbulent channel flows report the establishment of an equilibrium region above smooth and rough surface sections for strip widths 3δ and 6.28δ, respectively. In both cases, the rough strip is represented by a numerical roughness model. The boundary layer measurements of Wangsawijaya *et al.* (2020) find near-equilibrium conditions for strip width starting at 3.6δ, where roughness is realised with P36 grit sandpaper. To the authors' knowledge, the streamwise development length required to reach an equilibrium flow state over strip-type roughness has not been systematically investigated so far. For the development of turbulent secondary flows in open channel flows, Zampiron *et al.* (2023) report a development length of the order of 100 channel heights. This includes secondary flows that form due the presence of sidewalls as well as for those that are roughness-induced. An analysis of the temporal decay of turbulent secondary motions in channels (Andreolli *et al.* 2025) showed that the high- and low-momentum pathways generated by turbulent secondary motion take longer to decay than cross-sectional circulatory motions. Translated into a spatial decay, a decay length of the order of 20δ is reported.

For streamwise smooth–rough surface transitions, most focus was placed on the recovery length required to achieve equilibrium conditions downstream of a single step change in the boundary condition; see e.g. Hanson & Ganapathisubramani (2016) and Li *et al.* (2019). For turbulent boundary layers, a recovery length of the order of $20\delta-50\delta$ is reported (Devenport & Lowe 2022). Turbulent boundary layers over single rough strips aligned transversely to the main flow direction were studied experimentally by e.g. Andreopoulos & Wood (1982) and Jacobi & McKeon (2011). The repeated change of surface condition (smooth to rough and back to smooth) leads to the formation of two successive internal boundary layers that start at the leading and trailing edges of the roughness strip, respectively. A non-monotonic development of the friction coefficient downstream of the roughness strip was found with recovery length at least 10δ (Devenport & Lowe 2022). While all these investigations of a streamwise step change in boundary condition were carried out in (external) turbulent boundary layers, the response of a confined (internal) flow to a sudden onset of roughness was investigated by Van Buren *et al.* (2020). In contrast to external flows, mass conservation requires any change in the near-wall region to be balanced by the velocity profile further away from the wall, such that the centreline velocity of an internal flow instantly reacts to a step change in surface roughness. In terms of development length required to adapt to the new surface after a step change, and of a related non-monotonic transient behaviour, results comparable to those for turbulent boundary layers are reported.

Although different aspects of turbulent flow properties over heterogeneous rough surfaces have been studied (e.g. Jacobi & McKeon 2011; Vanderwel *et al.* 2019; Wangsawijaya & Hutchins 2022), the corresponding global drag and its Reynolds number dependence have hardly been addressed in the literature. Due to this lack of data, the quality of available drag prediction models cannot be evaluated. Recently, Jensen & Forooghi (2025) investigated the impact of different roughness patches (consisting of randomly placed truncated cones) on the friction coefficient of turbulent channel flow, with the goal to provide a framework to estimate the global drag of heterogeneous rough surfaces. This study is based on DNS at relatively low Reynolds number ($180 \leqslant Re_\tau \leqslant 520$). They report an asymptotic convergence towards results based on a prediction that assumes the validity of local equilibrium for patch sizes that are approximately one order of magnitude larger than δ. Within the investigated range, they find only a weak Reynolds

k_{avg} (mm)	k^r_{avg} (mm)	k_{rms} (mm)	k_s (mm)
0.67	0.37	0.08	0.78

Table 1. Roughness properties of P60 sandpaper: k_{avg} corresponds to the melt-down height of the entire sandpaper (including its base material), k^r_{avg} refers to the mean height of the rough surface part only (i.e. without the base material), k_{rms} is the RMS value of the surface height distribution, k_s corresponds to the equivalent sand grain height evaluated in such a way that the influence of the base material is excluded; see Frohnapfel *et al.* (2024).

number dependence of the global drag, but highlight the need for experimental data at higher Reynolds numbers.

In the present work, we start by considering a surface as heterogeneous when its statistical roughness properties change over a length scale that is of the order of the outer scale δ of the flow or larger. While this loose definition is in line with previous work (see e.g. Chung *et al.* 2021), a universal definition of heterogeneous roughness is still lacking. We present results of pressure-gradient measurements for six different surfaces with identical roughness coverage (50 % rough and 50 % smooth) but different roughness placement. Hot-wire measurements provide information about the corresponding flow fields. Through variation of the Reynolds number, the patch size of rough and smooth surface sections is varied in viscous units. The obtained results show that one and the same physical surface can be perceived as homogeneous or heterogeneous by the turbulent flow, depending on the Reynolds number. In analogy to the concept of a hydraulically smooth/rough surface, we introduce the notion of a hydraulically homogeneous/heterogeneous surface.

2. Experimental investigation

2.1. *Investigated surfaces*

We consider heterogeneous rough surfaces in which the statistical properties over relatively large patches remain constant. For the present investigation, surface patches are either smooth or covered with P60 grit sandpaper. The roughness properties of P60 sandpaper were evaluated in Frohnapfel *et al.* (2024) and are summarised in table 1.

In particular, we complement existing datasets for strip-type roughness composed of alternating smooth and rough strips with strip widths $s \approx \delta$ and $s \approx 2\delta$ (Frohnapfel *et al.* 2024) with narrower strips of $s \approx 0.5\delta$ and broader strips of $s \approx 4\delta$, where δ is the channel half-height of the experimental set-up described in the next subsection. In addition to these cases in which roughness strips are aligned in the streamwise direction, we consider strips of width 4δ aligned in the spanwise direction, and a checkerboard pattern with 4δ side length. All investigated surfaces are sketched in figure 1 and summarised in table 2. In addition to the heterogeneous rough surfaces, the reference cases of homogeneous smooth and homogeneous rough surfaces are also considered.

Since a varying net channel height due to roughness elevation poses a challenge for data evaluation, all surfaces are manufactured such that the mean height of the roughness is at the same elevation as the smooth surface part. To realise this, the locations where surface roughness is to be placed are first milled locally to produce valleys with depth k_{avg} (see table 1). In a second step, the laser-cut sandpaper patches are glued into these valleys. In this paper, all data evaluation is based on the geometrical mean channel height. This is one of the three options discussed in Frohnapfel *et al.* (2024). To keep a consistent data evaluation throughout all discussed results, the value for k_s reported in table 1 also corresponds to a data evaluation based on the mean channel height. If scaled

	Label	s (mm)	δ_{avg} (mm)	N	Colour
Homogeneous surfaces	Smooth	—	12.60	—	△
	Hom rgh	—	12.18	—	△
Strip-type surfaces	ST 0.5δ	6.125	12.67	24	△
	ST 1δ	12.5	12.71	12	△
	ST 2δ	25	12.66	6	△
	ST 4δ	50	12.69	3	△
Checkerboard surface	CH	50	12.67	3	△
Strips perpendicular	SP	50	12.67	1	△

Table 2. Overview of the investigated surfaces with the labels and colour code used in the figures. For each case, the strip width s and the measured mean channel half-height δ_{avg} is given, and N is the number of rough strips or squares, respectively, in the spanwise direction.

in viscous units, k_s reaches $k_s^+ \approx 70$ (which corresponds to the onset of the fully rough regime; Schlichting 1979) at bulk Reynolds number $Re_b = 28\,000$ in the experimental facility described in the next subsection. The hot-wire measurements presented in § 4.2 are taken at bulk Reynolds numbers $Re_b = 12\,000, 37\,000, 50\,000$, which correspond to $k_s^+ \approx 28, 94, 126$ for the homogeneous rough surface configuration.

2.2. *Experimental set-up*

The experimental set-up and procedure are the same as in previous work (e.g. Gatti *et al.* 2015; Frohnapfel *et al.* 2024). We operate an open-circuit blower wind tunnel, in which the channel flow test section (aspect ratio $AR = W/2\delta \approx 12$) is placed downstream of a settling chamber. The channel width $W = 300$ mm is identical for all investigated configurations (uncertainty $\delta W < 0.01$ %). The (mean) channel half-height δ_{avg} is measured for each configuration with underlaying uncertainty <0.1 %. The corresponding value for the smooth-wall reference case is used as reference length scale $\delta = 12.6$ mm in the present work (e.g. the strip width s is expressed in multiples of δ in the labelling of strip-type surfaces introduced in table 2). All measured values for the channel half-height are included in table 2. The smaller δ_{avg} for the homogeneous rough surface is due to a different manufacturing procedure. As mentioned above, all data evaluation (see §§ 3 and 4) is based on δ_{avg}.

The flow is tripped at the inlet of the test section, which has total length 3950 mm ($\approx 314\delta$), and develops along smooth channel walls for 2450 mm ($\approx 195\delta$). The last part of the test section is equipped symmetrically with the rough surfaces (symmetric arrangement on top and bottom of the channel with respect to channel centre). It has length $L = 1500$ mm ($\approx 119\delta$). All surfaces are designed in such a way that $W/2s$ is a natural number (as indicated in figure 1). The strip-type surface with $s \approx 4\delta$ (ST 4δ) encompasses only three roughness strips on each channel wall, while we have 24 rough strips on each wall for ST 0.5δ.

The pressure gradient along the rough channel is measured with pressure taps that are placed along both sidewalls in streamwise intervals of 200 mm. The static pressure at different streamwise locations is measured compared to a fixed reference location in the smooth channel section. Within the rough section, the resulting streamwise pressure gradient $\Pi = -\Delta p/\Delta x$ is evaluated over a length 1 m corresponding to 79δ, along which six consecutive measurement locations are placed. The first pressure tap (pair) used for the

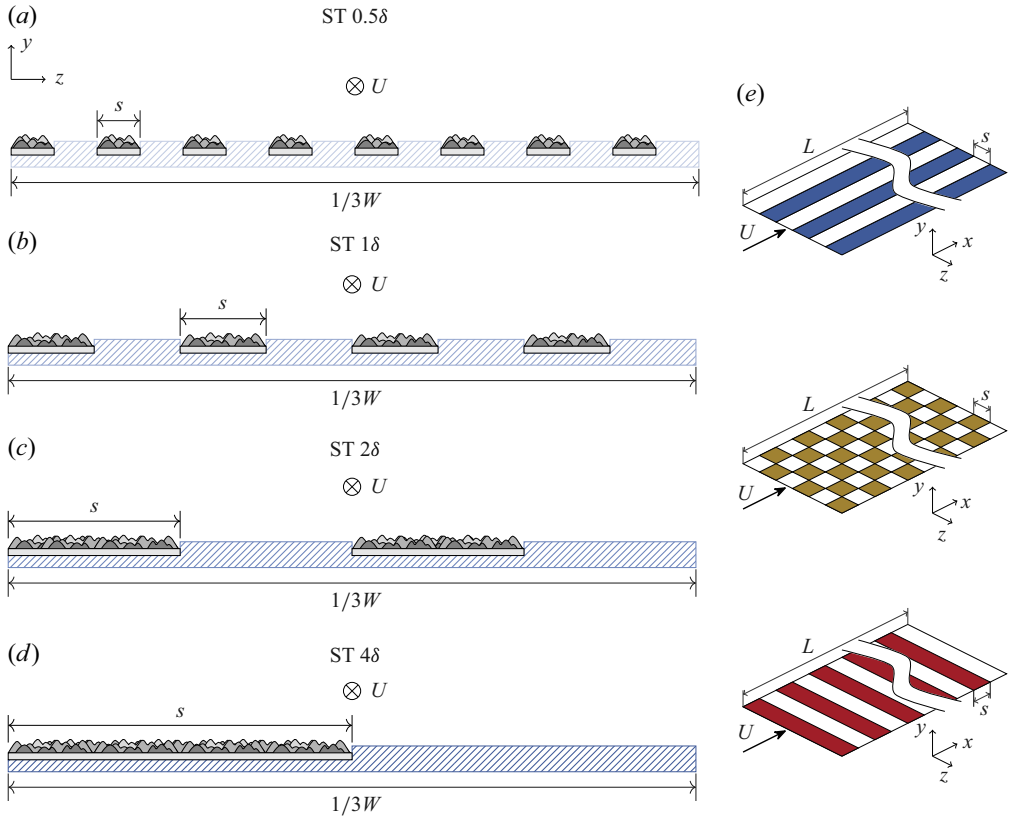

Figure 1. (*a–d*) Sketches of the investigated strip-type (ST) surfaces with strip widths $s \approx 0.5\delta$, 1δ, 2δ, 4δ. (*e*) Top view of the ST 4δ (top), the checkerboard (CH, middle) and the perpendicular (SP, bottom) strips surface configurations; in all cases, $s \approx 4\delta$. All surfaces have roughness coverage 50 %. The sketches' colours (shades of blue for ST, red for SP, yellow for CH) are used in figures 5 and 6 to represent the corresponding results.

evaluation of Π is placed 250 mm ($\approx 20\delta$) downstream of the start of the rough test section part; the last one is placed 250 mm upstream of the end of the channel. In this region, Π is determined by a least squares fit through the six consecutive data points. The maximum relative deviation of a data point from the fit was found to be 0.8 %. For the widest strip-type roughness and the checkerboard surface, the pressure-gradient measurements were also evaluated independently on each channel sidewall. No differences between the two channel sidewalls were found.

The mass flow rate $\dot{m}$ of the wind tunnel is measured on its suction side with an orifice flow meter installed in a long suction pipe. The mass flow rates are adjusted to cover Reynolds number range $4500 \leqslant Re_b \leqslant 75\,000$ in the channel flow test section (see § 3 for Reynolds number definition). To maintain the pressure drop across the orifice plates within the available measurement range, four different orifice plates are required. It was previously shown that results (in terms of C_f versus Re_b, as discussed in the following) obtained with a single orifice plate are highly reproducible, while deviations between the different orifice plates introduce larger scatter (Gatti *et al.* 2015). Therefore, results obtained with different orifice plates are reported with different symbols in the following. These are summarised in table 3. The corresponding uncertainty of the mass flow rate is $\delta\dot{m} < 2\,\%$. In addition to flow rate and pressure gradient along the channel test section,

Symbol	d_{in} (mm)	Re_b range
△	60	$4500 < Re_b < 13\,000$
◊	105	$9000 < Re_b < 38\,000$
○	120	$12\,500 < Re_b < 48\,000$
□	150	$22\,000 < Re_b < 75\,000$

Table 3. Symbols that represent the different orifice plates for the mass flow rate measurement, with their corresponding Reynolds number ranges. The inner diameter of each orifice plate is given by d_{in}.

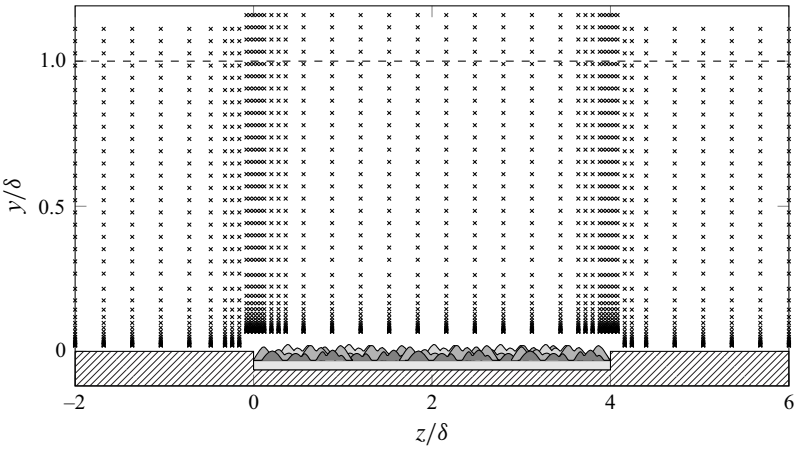

Figure 2. Example of hot-wire measurement positions above the 4δ strip-type surface. The dashed line represents the channel centreline, and $z/\delta = 0$ corresponds to the spanwise centre of the channel.

temperature and ambient pressure are monitored to obtain the fluid properties (density ρ and dynamic viscosity μ), the uncertainties of which are estimated to be 0.2 % (for ρ) and 0.05 % (for μ) (Gatti *et al.* 2015).

2.3. *Hot-wire anemometry*

The streamwise velocity distribution over the heterogeneous surfaces is measured in wall-normal planes by means of hot-wire anemometry. A corresponding measurement grid is shown in figure 2. It is refined in the near-wall region and has additional refinements in the spanwise direction in the vicinity of the smooth–rough transitions. Measurements are conducted at $Re_b = 12\,000$, 37 000, 50 000, with sampling times $T_{samp} = 26$, 10, 8 s (following the suggestion of Hutchins *et al.* 2009). The sampling frequency in all experiments is set to 60 kHz, combined with low-pass filter 30 kHz.

The measurements are conducted with a DANTEC 55P11 single-wire probe equipped with a tungsten wire with active sensing length of approximately 1.25 mm and diameter 5 µm. The probe is operated by a DANTEC StreamLine Pro 90N10 frame in conjunction with a 90C10 constant temperature anemometer module operated at fixed overheat ratio a_R of 80 %. An offset and gain are applied to the raw signal to cover the whole range of the 16-bit A/D converter used. Velocity calibration is performed *ex situ* in a pressure-driven jet before and after the measurements. Temperature changes during the run are recorded and accounted for by a temperature compensation as outlined in Örlü & Vinuesa (2017). The wall-normal and spanwise measurement positions are varied by means of two perpendicularly aligned Thorlabs LTS150/M automated axes.

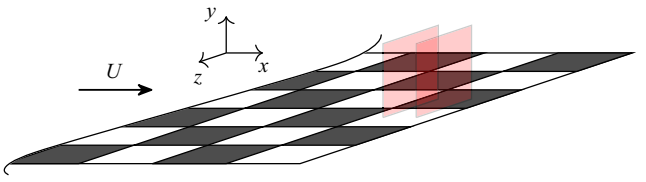

Figure 3. Sketch of the two measurement planes (in transparent red colour) above the checkerboard surface. Those two planes are located at a distance 5 mm (P1) and 30 mm (P2) downstream of a patch leading edge.

In the case of the strip-type surfaces, measurements are taken 15 mm upstream of the outlet of the test section. In earlier work, results from this measurement position were found to be trustworthy based on comparison with measurement data from further upstream locations and DNS data (Frohnapfel *et al.* 2024). For the checkerboard pattern, two different streamwise positions are considered, located on the last patches upstream of the test-section outlet. These two positions, referred to as P1 and P2 in the following, correspond to 5 and 30 mm behind the leading edges of the patches, as indicated in figure 3.

To measure streamwise variations in the centreline velocities over the surfaces with streamwise heterogeneity, i.e. the surface with perpendicular strips and the checkerboard surface, the centreline velocity is evaluated along a length 100 mm in steps of 5 mm, starting 10 mm before a rough-to-smooth step change, and ending 40 mm behind the following smooth-to-rough step change (thus 10 mm in front of the channel outlet). In the case of the checkerboard surface, this is done at two different spanwise positions: once in the spanwise centre of the patches, and once above the edge.

All velocity signals are averaged in time to obtain local mean and root mean square (RMS) values. Time-averaging is indicated by an overbar. In addition, a spanwise average over s or $2s$ at fixed wall-normal positions (indicated by angular brackets) is computed to obtain a dispersive mean velocity component

$$\tilde{u}(y, z) = \overline{u}(y, z) - \langle \overline{u} \rangle (y). \tag{2.1}$$

3. Non-dimensional pressure-gradient curves and idealised predictions

In order to enable a general comparability of the measured data, they need to be transferred into dimensionless numbers. The classical (Nikuradse-type) description of flow resistance for rough-wall internal flows relies on the bulk Reynolds number $Re_b = 2\delta U_b \rho/\mu$ and a friction coefficient that is either $C_f = 2\tau_w/(\rho U_b^2)$ or $\lambda = 4C_f$ (Schlichting 1979).

To deduce these non-dimensional variables from the measured quantities, we require the following definitions of bulk velocity and effective wall shear stress:

$$U_b = \frac{\dot{m}}{2\delta W \rho}, \quad \tau_w = \underbrace{-\frac{\Delta p}{\Delta x}}_{\Pi} \delta_{avg}. \tag{3.1}$$

Under the assumption of constant channel dimensions (W and δ_{avg}) and constant fluid properties (μ and ρ), the mass flow rate $\dot{m}$ is a direct measure for U_b, while the streamwise pressure gradient Π represents (a spatially averaged) τ_w. In consequence, Re_b is governed by $\dot{m}$, while the friction coefficient is a non-dimensional quantity in which both measured key quantities, $\dot{m}$ and Π, are combined:

$$Re_b = \frac{1}{W\mu}\dot{m}, \quad C_f = 8\delta_{avg}^3 W^2 \rho \frac{\Pi}{\dot{m}^2}. \tag{3.2}$$

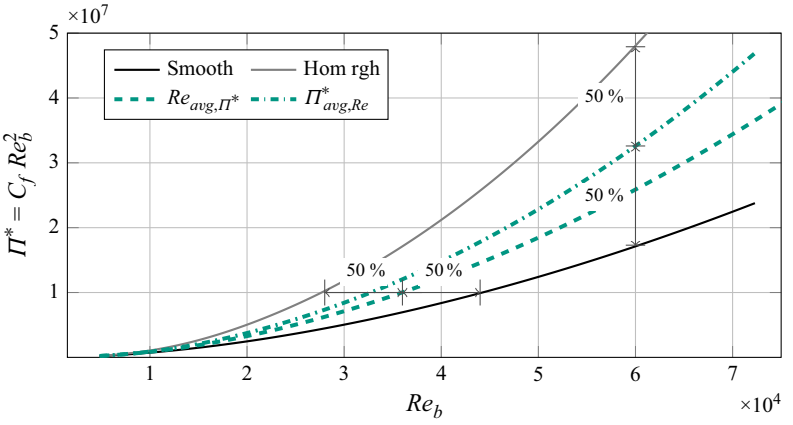

Figure 4. Homogeneous smooth and rough wall reference data in terms of Π^* versus Re_b, and idealised averages of these cases for rough surfaces with 50 % roughness coverage under the equilibrium assumption. The dashed line assumes the same streamwise pressure gradient to be present in all channel subsections (smooth and rough). Therefore, Re_b is averaged along a horizontal line to obtain a global drag prediction Re_{avg,Π^*}. The dash-dotted line assumes the same flow rate in all channel subsections. Hence Π^* at constant Re_b is averaged for $\Pi^*_{avg,Re}$. The arrows illustrate the two averaging procedures.

In order to obtain a dimensionless number that is governed by Π only, we consider

$$C_f\, Re_b^2 = \frac{8\delta_{avg}^3 \rho}{\mu^2}\Pi = \Pi^*. \tag{3.3}$$

This number is equivalent to the square of the friction Reynolds number Re_τ, except for a proportionality constant. In the context of internal flows, it has been used to compare different types of drag-reducing flow control approaches (Frohnapfel, Hasegawa & Quadrio 2012). It is also related to one of the non-dimensional variables in which the universal law of friction for smooth pipes is given; see Schlichting (1979), $Re_b\sqrt{\lambda} = 2\sqrt{\Pi^*}$. We denote this dimensionless number by Π^* to represent its physical meaning of a dimensionless pressure gradient.

For the present data evaluation, the uncertainties of all measured quantities ($\dot{m}$, Π, δ_{avg}, W, ρ, μ) can be combined via Gaussian error propagation, following the procedure outlined in Gatti *et al.* (2015). Based on a 95 % confidence level, we find the following uncertainty for the deduced dimensionless numbers: $\delta Re_b < 2\,\%$, $\delta C_f < 4\,\%$, $\delta\Pi^* < 2\,\%$.

Figure 4 depicts data of a smooth channel flow and a channel flow with P60 sandpaper placed on both walls in terms of Π^* versus Re_b. The black curve corresponds to the non-dimensional pressure gradient required to achieve a certain Re_b for a smooth-wall channel, while the grey curve represents the corresponding pressure gradient required with rough channel walls. For this plot, previously published measurement data obtained in the same facility (Frohnapfel *et al.* 2024) were interpolated with least squares fits to enable their use in simplified predictions for the global drag of surfaces that consist of smooth and rough patches. The representation nicely visualises the physics of an increased pressure gradient with increasing flow rate for both smooth and rough surfaces, as well as the increasing difference in pressure gradient between rough and smooth surfaces with increasing Reynolds number.

This particular representation allows including two idealised cases for global drag predictions of heterogeneous rough surfaces based on the equilibrium assumption in a

straightforward manner. An equilibrium condition between the flow and the surface is reached if the flow has fully adapted to the boundary condition prescribed at the surface such that it is locally in equilibrium with the underlying surface condition. For an idealised two-dimensional channel flow, this implies that all time-averaged quantities do not vary in the streamwise and spanwise directions. For the high-aspect-ratio channel flow considered experimentally, spanwise variations of mean flow quantities are limited to a region near the sidewalls such that a central part of the flow field does not exhibit any spanwise variation and provides a reasonable representation of the idealised two-dimensional channel flow (Vinuesa, Schlatter & Nagib 2015).

The equilibrium assumption, when applied to a channel flow, states that a patch of roughness produces a velocity profile identical to that generated over a rough surface with infinite extension in the streamwise and spanwise directions (at the same Re_b). In consequence, the relation $C_f(Re_b)$ or $\Pi^*(Re_b)$ obtained for a homogeneous rough surface is expected to hold over the rough patch. Any effects of patch edges are assumed to be negligibly small. Such an idealised consideration creates the opportunity to build a model for the global drag of heterogeneous rough surfaces by 'adding up' the drag of the subsurfaces.

For the channel flow configuration, two conceptually different ideas on how to 'add up' the subsurface drag properties can be formulated. The two results are included in figure 4. First, consider very large patches of rough and smooth subsurfaces that have a finite length in the streamwise direction but infinite extension in the spanwise direction (Jensen & Forooghi 2025). This is similar to the configuration placed lowest in figure 1(*e*), but with larger values of s. These surfaces are symmetrically placed on the top and bottom walls of a channel. Due to mass conservation, the same mass flow rate has to pass through channel sections bound by smooth walls and bound by rough walls. Hence the bulk Reynolds number is the same in both channel subsections. For any Re_b, we form the arithmetic mean of $\Pi^*_{smooth}(Re_b)$ and $\Pi^*_{rough}(Re_b)$ to represent the fact that 50 % of the channel surface is smooth, and 50 % is rough. This procedure is visualised by the vertical line in figure 4. It results in an idealised prediction for the global pressure gradient $\Pi^*_{avg,Re}$ of a channel with 50 % roughness coverage with P60 sandpaper which is represented by the dash-dotted line in figure 4.

The second idealised case considers very large patches of rough and smooth subsurfaces that have a finite extension in the spanwise direction but infinite extension in the streamwise direction (Neuhauser *et al.* 2022). This case is similar to the configuration shown in figure 1(*d*), but with larger values of s. For the flow to reach a fully developed state in a configuration in which alternating channel sections with smooth and rough wall are staggered in the spanwise direction, the streamwise pressure gradient along all channel sections has to be the same. In consequence, a different mass flow rate is found in smooth and rough channel sections: a larger flow rate passes through the channel section with smooth walls than with rough walls. The resulting global flow rate in terms of Re_{avg,Π^*} (dashed line in figure 4) is computed based on the mean value of $Re_{b,smooth}(\Pi^*)$ and $Re_{b,rough}(\Pi^*)$. We term this predictive curve the wide-strip limit of strip-type roughness. The corresponding averaging procedure is indicated by the horizontal line in figure 4.

The two idealised predictive curves for the global drag of heterogeneous rough surfaces diverge with increasing Reynolds number, with the wide-strip limit of strip-type roughness (Re_{avg,Π^*}) consistently below that based on a constant flow rate assumption ($\Pi^*_{avg,Re}$). In the present work, we compare these two idealised predictive curves with actual measurement data. The underlying assumptions of a local equilibrium between flow and surface, and negligible edge effects, are not expected to be valid. In fact, Neuhauser *et al.*

(2025) introduced a model extension for the wide-strip limit in which edge effects (spatial transients between equilibrium states) are considered. The extended model suggests that spatial transients lead to larger pressure gradients in a channel flow than indicated by the wide-strip limit. Irrespective of this known shortcoming of the simplest modelling approach, the degree of agreement of actual measurement data with such simple predictive approaches is of interest.

To evaluate the dimensionless pressure gradient of the heterogeneous rough surfaces in comparison to the smooth and homogeneous rough reference cases, we introduce a relative (dimensionless) pressure-gradient increase defined as

$$\Delta\Pi^*(Re_b) = \frac{\Pi^*_{het\ rough}(Re_b) - \Pi^*_{smooth}(Re_b)}{\Pi^*_{hom\ rough}(Re_b) - \Pi^*_{smooth}(Re_b)}. \tag{3.4}$$

This novel quantity sets the (Reynolds number dependent) difference in pressure gradient between the homogeneous rough and smooth surfaces ($\Pi^*_{hom\ rough} - \Pi^*_{smooth}$) as reference. It evaluates which percentage of this pressure-gradient increase due to surface roughness is realised with a heterogeneous rough surface. Since $\Delta\Pi^*$ is evaluated at constant Re_b, the idealised prediction of $\Pi^*_{avg,Re}$ (see vertical averaging procedure in figure 4) corresponds to $\Delta\Pi^* = 0.5$ by definition. In contrast, translating Re_{avg,Π^*} into $\Delta\Pi^*$ needs to be based on measurement data.

4. Results

4.1. *Friction coefficient and relative pressure-gradient increase*

Figure 5(*a*) shows the results for all strip-type rough surfaces (cf. table 2 and figure 1) in terms of C_f versus Re_b, compared to the smooth-wall reference data and the case where P60 sandpaper is homogeneously placed on both channel walls. Different colours represent different surface types, while different symbols correspond to different orifice plates used for the flow-rate measurements as indicated in table 3. Data are collected using different orifice plates whose operational Reynolds number ranges overlap. Therefore, the uncertainty in C_f that stems from the flow-rate measurement is clearly visible. The smooth-wall data closely follow the Dean correlation $C_f = 0.073\,Re_b^{-0.25}$ (Dean 1978), while the homogeneously rough case with P60 sandpaper shows a transitionally rough behaviour of Nikuradse type (i.e. converging towards an approximately constant value for C_f from below).

All data curves for strip-type surfaces show a similar behaviour in the sense that they are located in between the smooth and homogeneous rough reference, and do not appear to approach a constant C_f (and hence a fully rough regime) for large Re_b, but show a continuous slight decrease instead. Thus it is not possible to assign a k_s value to these surfaces. All datasets reveal a local minimum and maximum of C_f in their Reynolds number development around which C_f is approximately constant within a limited Re_b range. This general behaviour of the C_f curve was reproduced by Neuhauser *et al.* (2025) through a predictive model in which spanwise transients (edge effects) are added to the wide-strip limit. It is interesting to note that the relative drag levels of the different surfaces vary with Re_b. For example, at $Re_b \approx 12\,000$, ST 4δ yields the highest friction coefficient, and ST 0.5δ the lowest, while for $Re_b > 30\,000$, ST 1δ results in the highest and ST 2δ the lowest drag coefficients.

Figure 5(*b*) shows a comparison of the three surface types in which $s \approx 4\delta$ (see figure 1*e*). These are streamwise- and spanwise-aligned rough strips and the checkerboard configuration. The smooth and homogeneous rough data are again included

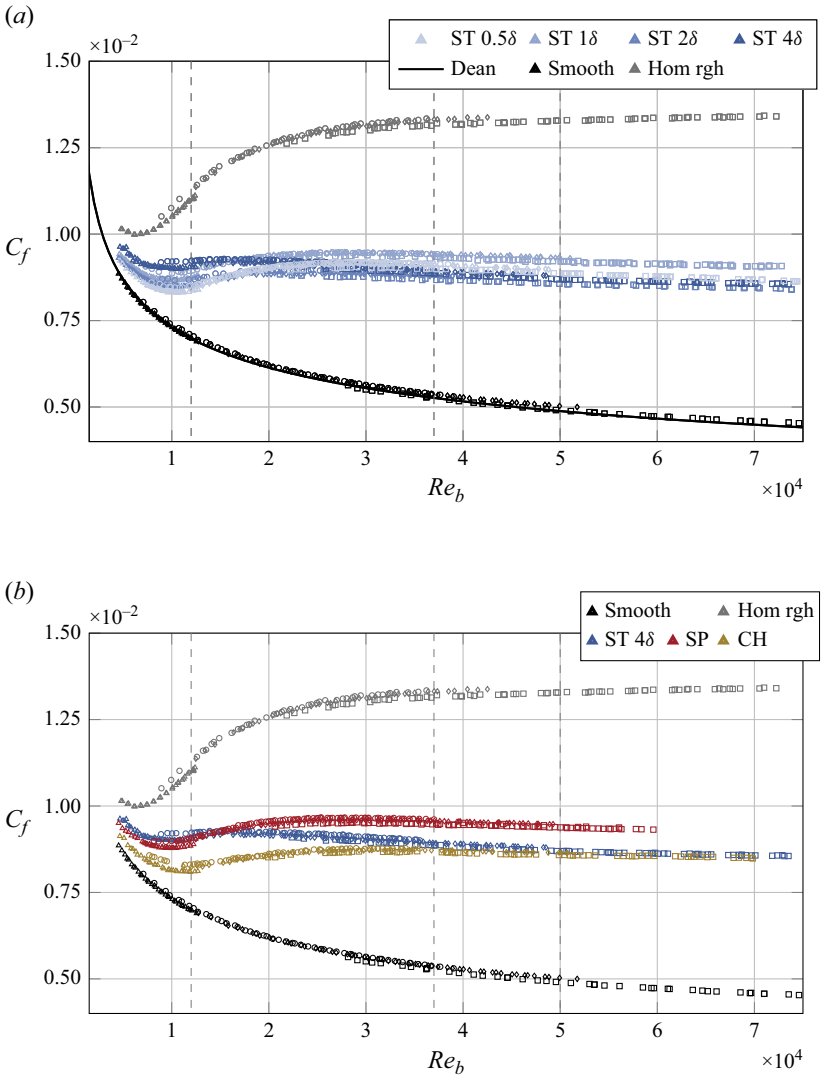

Figure 5. Friction coefficient C_f versus Re_b for the investigated surfaces jointly with data of the two homogeneous reference surfaces. In (*a*), the Dean correlation (Dean 1978) is added as additional reference for the smooth-wall channel flow. Different symbols represent different orifice plates in the mass flow rate measurement as indicated in table 3. The vertical dashed grey lines mark the three values of Re_b at which hot-wire measurements were taken (see § 4.2). (*a*) Friction coefficient C_f versus Re_b for the investigated strip-type surfaces. (*b*) Friction coefficient C_f versus Re_b for the three cases shown in figure 1(*e*), 4δ strip-type roughness, perpendicular strips and checkerboard pattern.

for reference. For these datasets as well, a distinct Reynolds number dependence of the global drag coefficient is visible. In the low Reynolds number regime, up to $Re_b \approx 20\,000$, the strip-type surface (ST 4δ) and the perpendicular strips (SP) show similar values for C_f, while the checkerboard surface (CH) yields lower drag coefficients. Starting at $Re_b \approx 40\,000$, the drag coefficient of CH basically collapses with that of ST 4δ, while SP results in a larger value of C_f. In addition, the general shape of the friction curve is more similar for SP and CH, with a clearly pronounced minimum in C_f at $Re_b \approx 10\,000$.

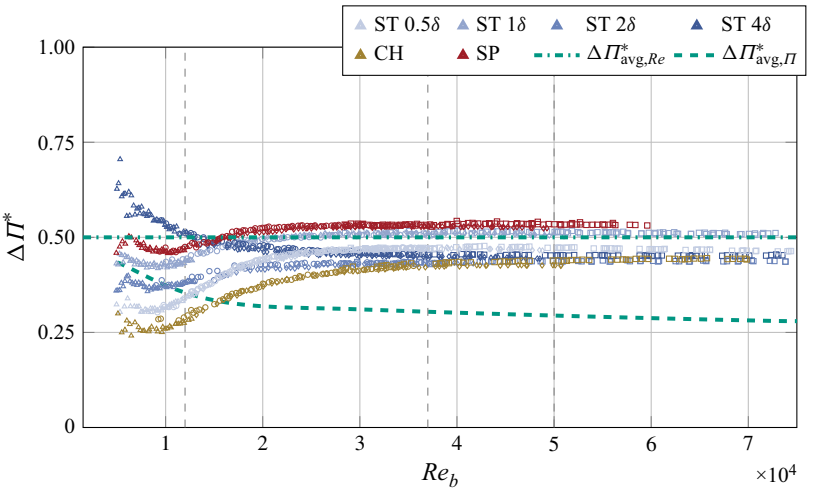

Figure 6. Relative pressure gradient increase $\Delta\Pi^*$ as a function of Re_b for all investigated surfaces. The idealised predictive curves for $\Delta\Pi^*_{avg,Re}$ and $\Delta\Pi^*_{avg,\Pi}$ are included for reference. Different symbols represent different orifice plates in the mass flow rate measurement as indicated in table 3. The vertical dashed grey lines mark the three values of Re_b at which hot-wire measurements were taken (see § 4.2).

The checkerboard surface (CH) displays the longest transient behaviour in the sense that its local maximum of C_f is reached at a higher Re_b than for the other surfaces.

Figure 6 shows the obtained results in terms of relative pressure-gradient increase $\Delta\Pi^*$ as introduced in (3.4). The data evaluation requires us to compare data for different surfaces at the same Re_b. In order to reduce the resulting uncertainty in the results, we only consider data obtained with the same orifice plate for the evaluation of $\Delta\Pi^*$. The figure also includes the idealised predictions of $\Pi^*_{avg,Re}$ and Re_{avg,Π^*} (see figure 4) translated into $\Delta\Pi^*$. We denote the former by $\Delta\Pi^*_{avg,Re}$, which takes on Reynolds-number-independent value 50 % by definition. The second idealised prediction is denoted by $\Delta\Pi^*_{avg,\Pi}$, and is introduced based on measurement data of the two homogeneous reference cases.

For high Re_b, all data curves for heterogeneous rough surfaces approach an approximately constant value in the $\Delta\Pi^*(Re_b)$ representation that is in the range $0.44 < \Delta\Pi^* < 0.53$. This result is in surprisingly good agreement with the idealised prediction for $\Delta\Pi^*_{avg,Re} = 0.5$, despite the fact that the underlying assumptions are not expected to be valid. The results clearly exceed the idealised prediction for $\Delta\Pi^*_{avg,\Pi}$. For strip-type roughness, this observation is in qualitative agreement with results by Neuhauser *et al.* (2025) that show that edge effects (which we expect to be present for the investigated surfaces) lead to an increased pressure gradient compared to Re_{avg,Π^*}.

The data for perpendicular strips (SP) settle on $\Delta\Pi^* = 0.53$, indicating that the pressure gradient of such a heterogeneous rough channel (with 50 % roughness coverage) is located at 53 % of the relative pressure-gradient difference between the homogeneous rough and homogeneous smooth cases, almost irrespective of the Reynolds number once a certain critical value of Re_b is surpassed. In contrast, the checkerboard surface (CH) approaches a value below $\Delta\Pi^* = 0.5$. All strip-type surfaces are located at $\Delta\Pi^*$ values below that of SP. Among the strip-type surfaces, the strip-type roughness with $s \approx \delta$ (ST 1δ) reaches the largest values for $\Delta\Pi^*$.

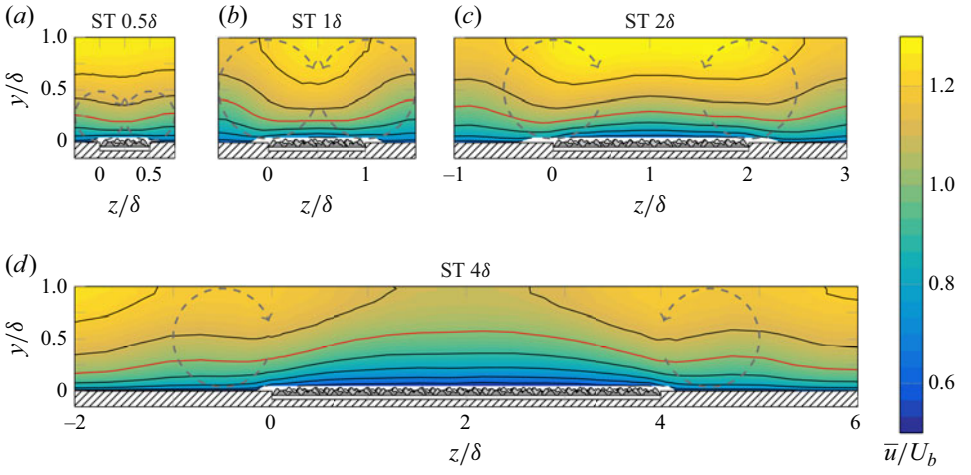

Figure 7. Contour plots of streamwise velocity over the strip-type surfaces at $Re_b = 37\,000$, where $z/\delta = 0$ marks the spanwise centre of the channel. Solid lines represent isovels, and the red line marks $\overline{u}/U_b = 1$. Conceptual sketches of the secondary motions are added as grey dashed arrows.

In their transient regime, the heterogeneous rough surfaces differ clearly. The strip-type surface ST 4δ approaches its limiting value from above (i.e. the global drag is more similar to the homogeneous rough than to the homogeneous smooth surface at lower Re_b); all other surfaces reveal a local minimum in $\Delta\Pi^*(Re_b)$ that is most pronounced for the checkerboard surface. The two surfaces that have the largest difference in $\Delta\Pi^*$ (30 % difference at $Re_b \approx 10\,000$ between ST 4δ and CH) both reach a value $\Delta\Pi^* = 0.45 \pm 0.01$ for $Re_b > 37\,000$. As noted before, CH undergoes the longest transient before settling on a nearly constant value for $\Delta\Pi^*$. These observations suggest that the flow field for CH transitions towards increased similarity with ST 4δ as the viscous length scale of the 4δ patch size grows. This anticipated similarity, however, is not supported by the flow-field measurements presented in § 4.2.

The fact that all investigated heterogeneous rough surfaces approach a nearly constant $\Delta\Pi^*$ with increasing Re_b has interesting implications for the prediction endeavours of flow resistance in channels with heterogeneous rough surfaces. Similar to the Reynolds-number-independent friction coefficient for (homogeneous) rough surfaces, it suggests that a single additional non-dimensional parameter is sufficient to describe the global drag behaviour.

With the goal to identify flow properties that characterise the different drag behaviours at lower and higher Re_b, we consider hot-wire data for different heterogeneous rough surfaces at $Re_b = 12\,000$ (minimum C_f for CH), $Re_b = 37\,000$ (end of transient regime for CH) and $Re_b = 50\,000$ in the following. These Reynolds numbers are marked in figures 5(*a*), 5(*b*) and 6.

4.2. *Hot-wire measurements*

4.2.1. *Streamwise-aligned roughness strips*

Results of hot-wire measurements over all strip-type surfaces are shown in figure 7 for $Re_b = 37\,000$. The colour code visualises the local time-averaged streamwise velocity component $\overline{u}$ normalised with the global bulk velocity U_b (see (3.1)) used to compute Re_b. The solid black lines correspond to isolines of $\overline{u}/U_b$, referred to as isovels in the following.

The results that show a pronounced spanwise variation of $\overline{u}$ are in agreement with literature results (e.g. Wangsawijaya *et al.* 2020) in the sense that the locations of high- and low-momentum pathways change their location with increasing strip width. Only for the widest strips ($s \approx 4\delta$) did we find larger flow speeds over the smooth surface sections, as one would expect to be the case if equilibrium conditions were achieved. The opposite location for high- and low-momentum pathways is found for smaller strip width, a phenomenon that is caused by the presence of turbulent secondary motions. These in-plane circulatory motions are initiated at the interphase between smooth and rough surface sections. For roughness strips of the order of the boundary layer thickness, secondary motions are known to lead to uplifting of near-wall fluid above the smooth surface sections, and to downwelling above the rough ones. Their presence is indicated by arrows with grey dashed lines in figure 7. We note that these are just conceptual sketches since the hot-wire data do not provide these velocity components. In the case of the widest strips (figure 7*d*), the imprint of the turbulent secondary flow can be seen by local minima and maxima of the isovels around the rough–smooth interface. The curved shape of the isovels above the centre of the rough patch reveals that – in contrast to some literature references (Wangsawijaya *et al.* 2020; Andreolli *et al.* 2025) – we do not reach a zone with equilibrium conditions in the centre of the 4δ patches, but find a local minimum centreline velocity at $z/\delta = 2$ (see figure 7*d*). It is likely that the approach towards an equilibrium condition in the strip centre is governed not only by s, but also by the type of roughness and the Reynolds number. The determination of such a threshold is beyond the scope of the present investigation.

For the strip-type roughness ST 2δ, the isovels start to show an upward bulging over the rough surface section, which is most pronounced around $y/\delta = 0.5$, and weakens towards the centreline, where a region of approximately constant centreline velocity is found ($0.8 < z/\delta < 1.2$). The strongest bulging of isovels, and hence the strongest spanwise variation, is found for ST 1δ (see figure 7*b*) which is in good agreement with literature results. The highest centreline velocity is located above the centre of the rough patch, and the lowest one above the centre of the smooth patch. For ST 0.5δ, the isovel bulging is weak (due to the smaller extent of the turbulent secondary flow in this case), in particular further away from the wall.

In combination with the pressure-gradient measurements, it becomes evident that the markedly different mean flow distributions of cases ST 0.5δ, ST 2δ and ST 4δ at $Re_b = 37\,000$ do not significantly affect $\Delta\Pi^*$. With respect to case ST 1δ, we find the strongest isovel bulging (and hence the strongest flow heterogeneity in terms of $\partial\overline{u}/\partial z$), which co-occurs with the largest values of $\Delta\Pi^*$. In addition, all flow fields reveal clear deviations from local equilibrium conditions (indicated through curvature of the isovels), which confirms that the simplifying assumptions for $\Pi^*_{avg,Re}$ and Re_{avg,Π^*} are not met.

In the transitional regime at lower Reynolds number, larger differences between the different strip-type surfaces are found in terms of $\Delta\Pi^*$. Those are most pronounced for cases ST 0.5δ and ST 4δ. Therefore, the flow fields of these two cases at $Re_b = 12\,000$, $37\,000$ and $50\,000$ are compared in the following. In order to visualise the flow-field evolution in terms of spanwise heterogeneity with varying Re_b, we present the data in terms of the dispersive mean velocity $\tilde{u}$ (see (2.1)).

Figure 8 shows, in agreement with the flow-field visualisation of figure 7(*a*), that ST 0.5δ reveals positive values for $\tilde{u}$ over the rough surface sections, and negative values over smooth surface parts in the near-wall region, while $\tilde{u} \approx 0$ further away from the wall. The flow-field heterogeneity at $Re_b = 12\,000$ is significantly weaker than at the two higher Reynolds numbers, which show a clear similarity in terms of $\tilde{u}/U_b$, indicating that the

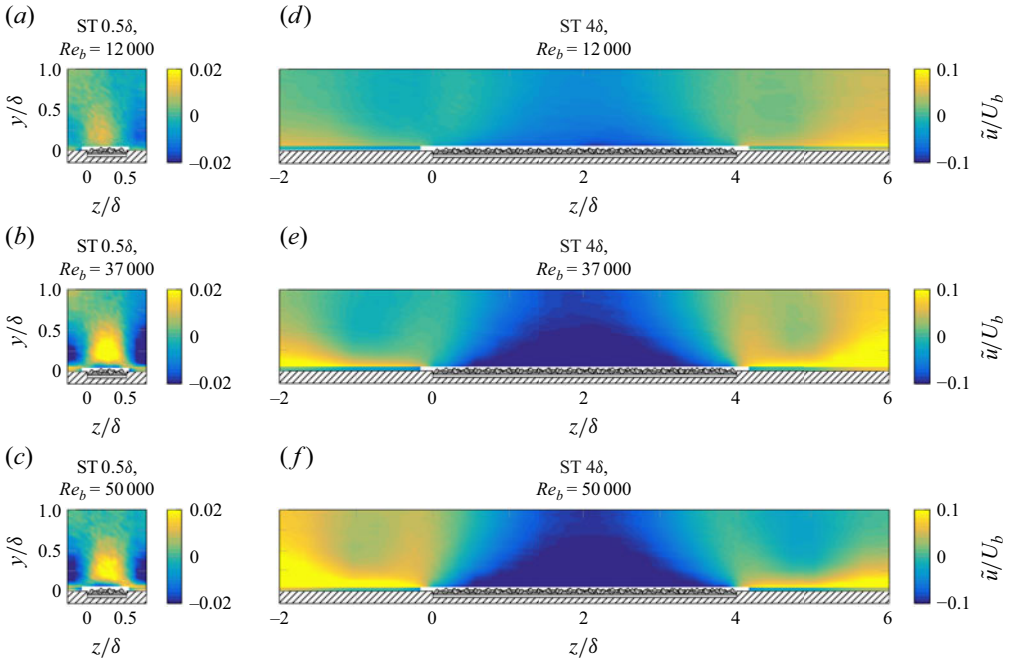

Figure 8. Spatial distribution of normalised dispersive velocities in terms of $\tilde{u}/U_b$ above the ST 0.5δ and ST 4δ surfaces at $Re_b = 12\,000$, 37 000 and 50 000; $z/\delta = 0$ marks the spanwise centre of the channel. Note that the colour bars differ for ST 0.5δ and ST 4δ.

increase in $\tilde{u}$ is similar to the increase in U_b. In the case ST 4δ, the dispersive velocities are almost one magnitude larger, and their spatial distribution is swapped: negative values of $\tilde{u}/U_b$ are located over the rough section, and positive ones over the smooth section. The imprint of the turbulent secondary flow is clearly visible in regions $-1 < z/\delta < 0$ and $4 < z/\delta < 5$. Similar to the ST 0.5δ case, it is also observed that the dispersive velocity in terms of $\tilde{u}/U_b$ is comparatively weak for $Re_b = 12\,000$, while a stronger and more similar flow heterogeneity is found for the two larger Re_b values. We note that the slight asymmetry of ST 4δ (around the centre of the rough patches), combined with the near-mirror-image appearance of the flow field at $Re_b = 37\,000$ compared to $Re_b = 50\,000$, most likely indicates that the flow statistics have not fully converged, particularly in the region of the turbulent secondary flow (see sketch in figure 7), which is known to exhibit slow dynamics (Vanderwel *et al.* 2019; Wangsawijaya & Hutchins 2022). Irrespective of this shortcoming, a clear trend towards an increasing self-similarity in the flow heterogeneity at the two largest Re_b can be discerned. This trend is also found for the other two strip-type surfaces (not shown here), which suggests that the Re regime in which $\Delta\Pi^*$ is almost constant for each surface (see figure 10 below) is characterised by self-similar velocity fields with regard to $\tilde{u}/U_b$.

The fact that the limiting value of $\Delta\Pi^*$ for large Re_b is approached from below for all strip-type surfaces except for ST 4δ is likely to be related to the different distributions of $\tilde{u}/U_b$. Exclusively negative values are located over the rough surface strips for ST 4δ, while the opposite is found for all other strip-type surfaces. The enhanced flow heterogeneity with increasing Re_b in the transitional regime thus indicates a relative flow speed decrease over the rough surface section for ST 4δ, which coincides with a reduction of $\Delta\Pi^*$, while a relative flow speed increase over the rough parts for ST 0.5δ (and the other two strip-type surfaces) coincides with an increase of $\Delta\Pi^*$. This observation aligns

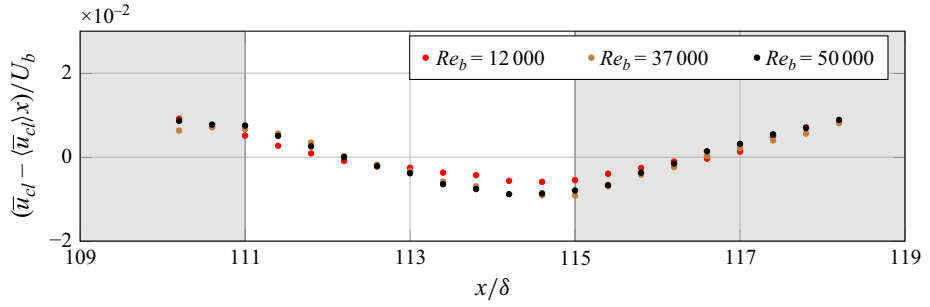

Figure 9. Development of the centreline velocity in the streamwise direction above the surface with perpendicular strips; $x/\delta = 0$ corresponds to the streamwise location in the channel at which the heterogeneous surface starts. The grey shading marks the region of the rough strip.

with the intuitive understanding that (relatively) higher flow velocities over the rough-wall sections induce larger flow resistance and hence larger relative pressure-gradient increase.

The data for each individual strip-type roughness suggest that similar flow fields are related to a similar relative pressure gradient increase. The observed differences at low Re_b might thus be interpreted as transitional heterogeneity, in some sense similar to a transitionally rough behaviour of homogeneous rough surfaces. However, it must be noted that the flow fields of ST 0.5δ, ST 2δ and ST 4δ differ significantly while resulting in basically the same pressure gradient. The flow-field difference is mainly related to the different topology of the turbulent secondary motion in these cases, suggesting that there is only a small relevance of turbulent secondary flow for flow resistance. Similar conclusions have previously been reported for turbulent secondary motions in duct flows (Pirozzoli *et al.* 2018). The slightly larger pressure gradient found for ST 1δ at high Re_b might be related to a particularly strong flow-field inhomogeneity (in terms of $\partial\overline{u}/\partial z$) induced by the turbulent secondary flow. This hypothesis provides a potential link to drag increase over riblet or ridge-type surfaces for which a significant drag contribution due to turbulent secondary flow has been reported (Stroh *et al.* 2020; Modesti *et al.* 2021). The turbulent secondary flow that emerges over such ridge-type surfaces with triangular cross-section is known to be characterised by strong localised upwash above the ridge tips (Zhdanov, Jelly & Busse 2024), which induces significant spanwise gradients of the streamwise mean flow field.

4.2.2. *Spanwise-aligned roughness strips*

Spanwise-aligned roughness strips in internal flows are expected to show a flow response to the step change in roughness over the entire velocity profile due to continuity, as discussed by Van Buren *et al.* (2020). The streamwise evolution of the centreline velocity $\overline{u}_{cl}$ (at $z = 0$) for surface SP is shown in figure 9 for $Re_b = 12\,000$, $37\,000$, $50\,000$ along a length $s = 8\delta$. Results are presented in terms of the relative deviation from the ensemble average of the measurement values at each Re_b, where the ensemble average is denoted by $\langle\overline{u}_{cl}\rangle_x$. We note that two individual data points are missing in the plot. Those were found to produce extreme outliers during the data evaluation, and were thus removed.

The data for all Re_b show similar trends: the flow decelerates on the channel centreline over the smooth strip, and accelerates over the rough strip. The highest centreline velocities are obtained slightly upstream of the change from rough to smooth strip in all cases. This is consistent with the expectation that near-wall fluid accelerates over the smooth surface section and decelerates over the rough one. The corresponding flow-field inhomogeneity is significantly weaker than for streamwise-aligned strips. The maximum local deviation

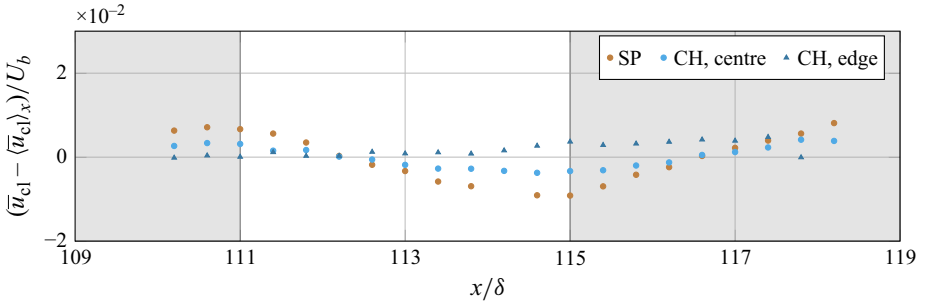

Figure 10. Comparison of the streamwise development of the centreline velocity above the perpendicular strips and above two positions on the checkerboard pattern – namely in the spanwise centre ($z/\delta = 0$) and at the edges of the patches ($z/\delta = 2$), $Re_b = 37\,000$.

from $\langle \overline{u}_{cl} \rangle_x / U_b$ is of the order of 1 % only. At $Re_b = 12\,000$, the results indicate a slightly smaller inhomogeneity. Thus, in agreement with the previous observations for strip-type surfaces, lower values of Π^* for one particular heterogeneous surface (SP in this case) are found to co-occur with reduced flow-field heterogeneity.

4.2.3. *Checkerboard pattern*

The checkerboard pattern (CH) combines the streamwise and spanwise surface inhomogeneities of the ST and SP surfaces. Hot-wire measurements were taken along the channel centreline at different spanwise positions to allow a comparison with SP, and in cross-planes at different streamwise positions to compare with ST 4δ.

The streamwise evolution of the centreline velocity over the checkerboard pattern is shown in figure 10 at $Re_b = 37\,000$. It is measured at a spanwise location along the centres of smooth and rough patches ($z/\delta = 0$), and at a spanwise location along the patch edges ($z/\delta = 2$). It can be seen that the consecutive acceleration and deceleration observed above perpendicular strips is present in the patch centres in a weaker form. Along the patch edges, the flow field is more homogeneous than along the patch centreline.

The impression of a rather homogeneous flow field over the checkerboard surface is also confirmed when considering cross-sections of the (streamwise) flow field as shown in figure 11 for two different streamwise positions. The measurement locations are placed 5 mm (position P1) and 30 mm (position P2) after the step change in surface property (where all smooth and rough patches have side length $s = 50$ mm).

As for the ST 0.5δ case, flow heterogeneity is least pronounced in the transitional regime ($Re_b = 12\,000$) where the lowest friction coefficient is found. At the two larger Re_b, for which $\Delta\Pi^*$ is very similar, the flow fields provide a self-similar impression in terms of $\tilde{u}/U_b$ that also aligns with results for streamwise-aligned roughness strips. At both measurement positions, the largest streamwise velocity is found over the smooth–rough interface around $z/\delta = 0$. However, the flow heterogeneity remains weak, with $|\tilde{u}/U_b|$ reaching maximum value 1 %. Thus the expectation that the flow field above the CH surface would become similar to the ST 4δ case at Reynolds numbers exhibiting very similar pressure gradients ($Re_b > 37\,000$) cannot be confirmed. Consequently, consistent with the results for the different strip-type surfaces discussed above, turbulent secondary motions do not appear to play a significant role in determining the pressure gradient in channel flow.

A distinct difference between P1 and P2 can be seen in the wall vicinity over the rough surface section ($0 < z/\delta < 2$). Fast-moving fluid ($\tilde{u} > 0$) is clearly visible at P1, which is located close to the upstream edge of the rough patch. Further downstream at P2, this

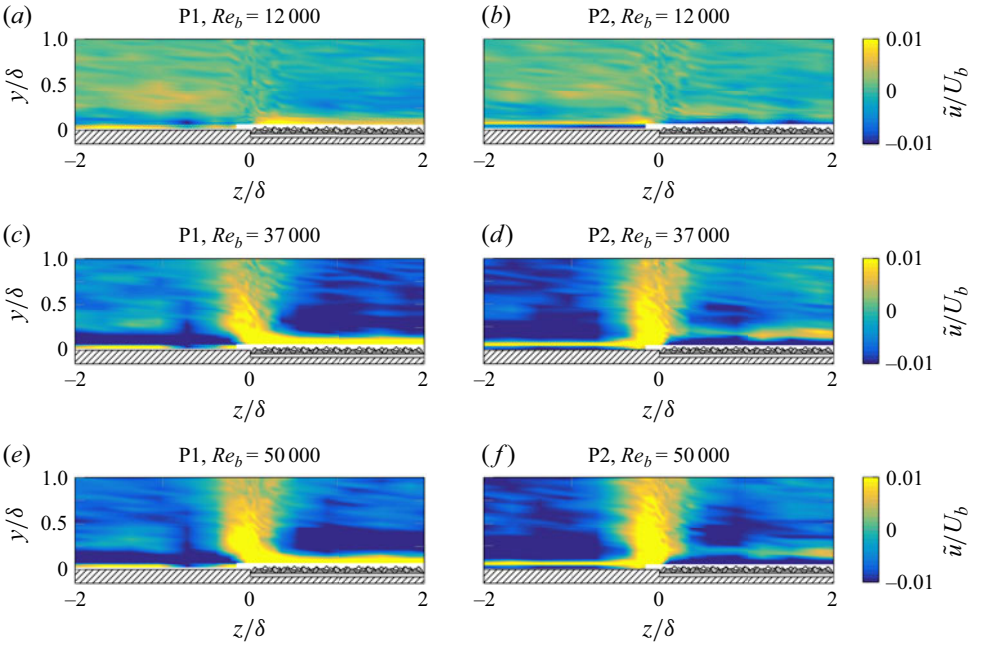

Figure 11. Dispersive velocities above the checkerboard surface, for each Reynolds number ($Re_b =$ 12 000, 37 000, 50 000) at positions P1 (*a*,*c*,*e*) and P2 (*b*,*d*,*f*), where $z/\delta = 0$ marks the spanwise centre of the channel.

near-wall region is occupied with slow-moving fluid. This deceleration over the rough surface patch is expected as the internal boundary layer over the rough patch develops. Simultaneously, a slight acceleration in the flow field further away from the wall is visible. Opposite trends can be seen over the smooth surface section ($-2 < z/\delta < 0$): near-wall fluid is accelerated from P1 to P2, while fluid further away from the wall is decelerated. These alternating flow states above the consecutive smooth and rough patches enclose the (weak) high momentum pathway at the smooth–rough interface.

The repeated formation of internal boundary layers is also clearly visible in the RMS value of streamwise velocity fluctuations. Due to the filtering effect of the hot wire, velocity fluctuations are not expected to be fully resolved for the present data, but a qualitative impression can be obtained as in Jacobi & McKeon (2011). The corresponding contour plots in terms of u_{rms}/U_b are shown in figure 12. At $Re_b = 12\,000$ (figures 12*a*,*b*), the isolines of u_{rms}/U_b approach the wall over the rough patch at P1, and move away from it at P2. In this plot, the values for u_{rms}/U_b decrease with increasing wall distance. Therefore, the shape of the isolines indicates slightly more intensive velocity fluctuation over the rough part at P2, while this is not the case at P1. This difference is related to the fact that the internal boundary layer that carries the increased RMS values over the rough surface part needs some streamwise distance to develop (similar to the observation for the mean flow field). Position P1 basically shows the RMS distribution of the upstream patches, for which the smooth section is located at $0 < z/\delta < 2$.

At the two higher Re_b values, a different picture emerges. Above the smooth surface sections, u_{rms}/U_b does not decrease continuously with increasing wall distance, but a region of elevated stress level exists around $y/\delta = 0.2$ at P2. In reference to Jacobi & McKeon (2011) on spanwise-aligned roughness strips in turbulent boundary layers, we refer to this region as a stress bore. At the start of the smooth patch, the new internal

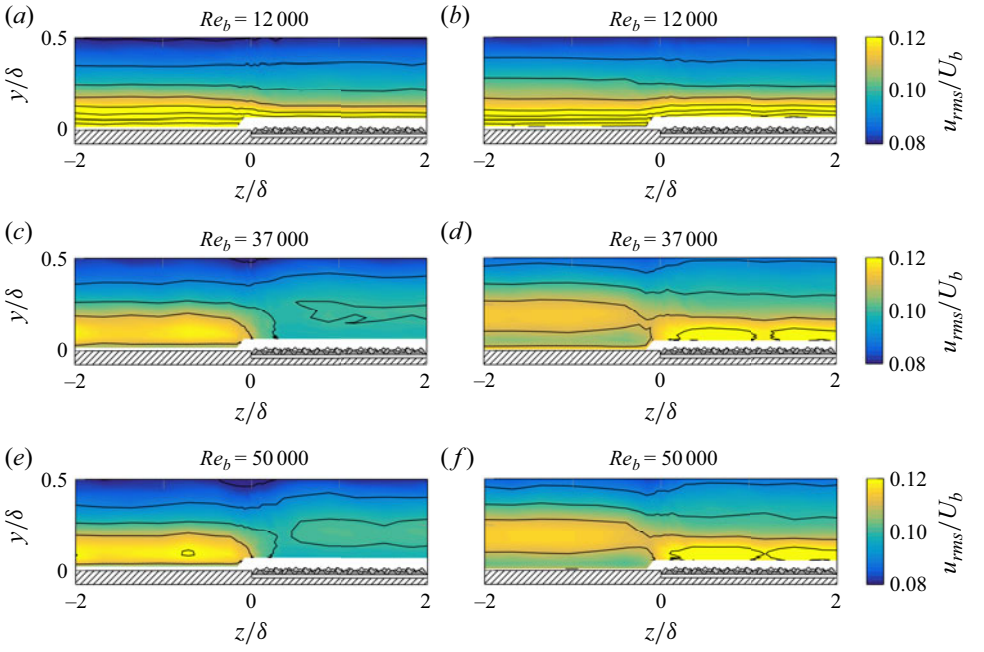

Figure 12. Isocontours of u_{rms}/U_b for the checkerboard surface at two different streamwise measurement positions (*a*,*c*,*e*) P1 and (*b*,*d*,*f*) P2 (see figure 3) at three different Re_b values, where $z/\delta = 0$ marks the spanwise centre of the channel.

boundary layer shifts the stress bore further away from the wall. This displacement mechanism can nicely be seen when comparing the data at P1 and P2. Indications of displaced stress bores are also visible over the rough sections ($0 < z/\delta < 2$) at both streamwise positions.

Turbulent secondary flow is known to be driven by cross-stream gradients of normal Reynolds stresses (Hinze 1973). For the present case, the repeated formation of internal boundary layers yields opposing spanwise gradients of the streamwise normal stress at different wall-normal locations. In consequence, there is no clear driving direction for the development of turbulent secondary flows such that the checkerboard surface pattern might be particularly resistant to the formation of these large-scale flow structures. It is likely that the emergence of the high-momentum pathway around $z/\delta = 0$ is directly linked to the 'alternating' stress bores, as both are observed only at the two higher Reynolds numbers.

The similarity of the mean flow fields at $Re_b = 37\,000$ and $Re_b = 50\,000$ is also confirmed in the RMS values, while the absence of stress bores for $Re_b = 12\,000$ suggests that the flow perceives the CH surface with characteristic length scale $s \approx 4\delta$ almost as an effective homogeneous boundary condition. This observation suggests that surface heterogeneity translates into flow heterogeneity once the patch size exceeds characteristic near-wall turbulent flow scales. At $Re_b = 12\,000$, the patch length and width of the checkerboard surface corresponds to $s^+ = su_\tau/\nu \approx 1600$, with the friction velocity u_τ being evaluated from the global τ_w defined in (3.1). Very weak flow inhomogeneity is also found for ST 0.5δ at $Re_b = 12\,000$. In this case, the strip width 0.5δ corresponds to $s^+ \approx 200$, while its length can be considered as infinite. The results indicate that the (viscous-scaled) threshold beyond which surface heterogeneity manifests in the flow is different for patchy surfaces compared with surfaces featuring only spanwise heterogeneity, a difference that likely arises from the anisotropic character of near-wall turbulence.

5. Discussion and conclusion

In the search for suitable predictive options for the global drag of heterogeneous rough surfaces, reference data are urgently required. We present measurement data for turbulent channel flows in the Reynolds number range $4500 \leqslant Re_b \leqslant 75\,000$. All data considered in the present work correspond to surfaces made up of patches with constant statistical properties. These rough and smooth surface patches cover 50 % of the total surface area each, and are arranged in a regular fashion that introduces a fixed length scale s in the range $0.5 < s/\delta < 4$.

Pressure-gradient and flow-rate measurements are used to deduce $C_f(Re_b)$ curves for six different heterogeneous rough surfaces. In all cases, no Reynolds-number-independent C_f is found, which is characteristic for the fully rough state in which an equivalent sand grain height k_s can be evaluated. An alternative data representation in terms of a relative pressure-gradient increase $\Delta\Pi^*$ as defined in (3.4) is found to be largely unaffected by Reynolds number once a surface-specific critical Re_b is surpassed. Up to this critical Re_b, the data show a significant Reynolds number dependence, which suggests that conclusions about the flow resistance of heterogeneous rough surfaces obtained at low Reynolds number (which is easily accessible in DNS) might be misleading for the extraction of trends that are used to build predictive models.

Complementary flow-field measurements reveal that this Reynolds number dependence is related to how the surface heterogeneity is perceived by the turbulent flow. A surface that leads to an almost homogeneous flow field at low Re_b can generate a heterogeneous flow field at higher Re_b. In addition, the heterogeneity of the flow field appears to approach a self-similar state that coincides with the tendency towards a constant relative pressure-gradient increase. Based on these observations, we suggest introducing the concept of a hydraulically heterogeneous surface in analogy to the well-established hydraulically rough surface that requires $k_s^+ > 5$ (Schlichting 1979). A patchy surface is hydraulically heterogeneous once the patch size exceeds particular thresholds. These thresholds appear to differ for surfaces with heterogeneity in both spatial directions, and for surfaces with spanwise heterogeneity only (strip-type roughness), which might reflect the anisotropy of near-wall turbulence in which turbulent structures are known to be elongated in the streamwise direction (Jiménez & Pinelli 1999). Once these thresholds are exceeded, the flow is transitionally heterogeneous, and its heterogeneity increases with Re_b before it reaches the fully heterogeneous state at the critical Reynolds number beyond which $\Delta\Pi^* \approx const$. The latter flow state is characterised by a self-similarity of the dispersive velocity field, determined in terms of $\tilde{u}/U_b$ in the present work.

This novel concept of a hydraulic-based definition for surface heterogeneity needs to be cross-checked in future work with further experimental and numerical data. In particular, thresholds for the onset of the transitionally and fully heterogeneous regime remain to be systematically investigated to assess whether a scaling framework can define universal thresholds that do not depend on the specific heterogeneous surface geometry.

In the fully heterogeneous regime, the measurement data yield a relative pressure-gradient increase in the range $0.44 < \Delta\Pi^* < 0.53$ for all considered surfaces. These results are in surprisingly good agreement with a very simple prediction in which the arithmetic average of the smooth- and rough-channel pressure gradient at constant Re_b is computed ($\Delta\Pi^*_{avg,Re} = 0.5$). This idealised prediction assumes step changes from one equilibrium condition to the other (i.e. negligible edge effects) in combination with identical flow rates per unit width in smooth- and rough-walled channel sections. The flow fields measured, which differ markedly among the investigated heterogeneous surfaces, confirm the expectation that both assumptions are not fulfilled in any of the cases.

It remains to be investigated in future work whether a similarly good agreement with the oversimplified prediction (which is identical to the use of an area-averaged C_f at constant Re_b) is also found for other heterogeneous rough surfaces.

Among the six investigated heterogeneous surfaces, four (ST 0.5δ, 2δ, 4δ and CH) yield $\Delta\Pi^* = 0.46 \pm 0.02$ in the fully heterogeneous regime, while two datasets (ST 1δ and SP) show larger relative pressure-gradient increase $\Delta\Pi^* = 0.52 \pm 0.01$. The similar pressure gradients for four surfaces that carry very different or no turbulent secondary flows suggest that these have little relevance for the flow resistance in channel flows – a conclusion that was previously also drawn for turbulent secondary motions in square ducts (Pirozzoli *et al.* 2018). In contrast, the larger $\Delta\Pi^*$ for ST 1δ might be related to an increased level of spanwise flow heterogeneity in terms of $\partial\overline{u}/\partial z$, which is also found for turbulent flow over streamwise-aligned ridges (riblets) in which turbulent secondary motions are understood to have a significant contribution to the overall drag (Stroh *et al.* 2020; Modesti *et al.* 2021).

The present study does not include full flow fields of the SP surface. This is the only one among the investigated heterogeneous surfaces in which the assumption of identical flow rates per unit width in smooth and rough channel sections is fulfilled by design. Measurements along the channel centreline reveal a streamwise modulation of the centreline velocity, which indicates the presence of non-negligible edge effects. Apparently, those lead to additional pressure-gradient requirements and thus to $\Delta\Pi^* > 0.5$.

In the transitionally heterogeneous regime, $\Delta\Pi^*$ shows larger differences between the different surfaces. Flow-field measurements at $Re_b = 12\,000$ reveal that the two surfaces that generate the lowest pressure gradients (CH and ST 0.5δ) induce almost homogeneous flow fields. Larger pressure gradients are related to more heterogeneous flow fields. For all surfaces, the fully heterogeneous value for $\Delta\Pi^*$ is approached from below with increasing Re_b, except for ST 4δ. This case is characterised by a different type of increasing flow heterogeneity in the sense that the magnitude of a negative $\tilde{u}$ (relatively slow flow speed) increases over the rough surface area. In other words, the flow rate per unit width in the rough channel section decreases with increasing Re_b such that a larger part of the flow rate can avoid the high-drag (rough) channel sections and passes through the channel sections with smooth walls. This behaviour is conceptually similar to the simplified prediction that assumes constant pressure gradient in smooth and rough parts of a strip-type surface, which also shows a continuous decrease of $\Delta\Pi^*$ with Re_b, but at lower values ($\Delta\Pi^*_{avg,\Pi}$ in figure 6). Again, edge effects (which are clearly visible in the flow fields) appear to induce larger pressure-gradient requirements for the same flow rate. The fact that all other heterogeneous surfaces also show a decrease of $\Delta\Pi^*$ with Re_b for $Re_b < 10\,000$ cannot be explained without flow-field data. It is possible that we see traces of the laminar flow state over the heterogeneous surfaces in this low-Reynolds-number regime.

In conclusion, the present study reveals that δ-scale surface heterogeneity can be perceived as an (almost) homogeneous boundary condition by a turbulent channel flow at low Reynolds number, and develop into flow heterogeneity at larger Re_b. This observation points towards a relevance of viscous flow scales for hydraulic heterogeneity. While this concept is similar to the onset of hydraulic roughness, it involves wall-parallel length scales rather than wall-normal ones, and the presented results indicate that the associated thresholds differ in streamwise and spanwise directions, and potentially interact with each other. In addition, flow heterogeneity is found to increase up to a certain Re_b, beyond which almost self-similar mean flow fields for each surface in terms of $\tilde{u}/U_b$ co-occur with almost constant relative pressure-gradient increase $\Delta\Pi^*$, a newly introduced metric. In this fully heterogeneous regime, different heterogeneous surfaces induce significantly

different mean flow fields but similar global pressure gradients, which is in agreement with an oversimplified pressure-gradient prediction. Future work incorporating additional data will be required to determine whether this surprising agreement is coincidental. For the surfaces investigated in the present study, the similarity of the measured pressure gradients suggests that turbulent secondary motions generated by strip-type surfaces have little relevance for global drag.

As noted in the Introduction, it is unlikely that observations made in internal flows with the present type of heterogeneous surfaces can directly be transferred to external flows. The introduced concept of hydrodynamic heterogeneity is expected to also hold for turbulent boundary layers, and remains to be investigated in this context.

Acknowledgements. The authors would like to acknowledge fruitful discussions with S. Dalpke, D. Gatti and J. Neuhauser, as well as the reviewers' constructive feedback.

Funding. This project is funded through the German Research Foundation DFG, project no. 521110788. P.S. acknowledges financial support through the Alexander von Humboldt foundation (project 1233956).

Declaration of interests. The authors report no conflict of interest.

Author contributions. C.S.: conceptualisation, data curation, investigation, validation, visualisation, formal analysis, project administration, writing. P.S.: conceptualisation, data curation, investigation, formal analysis, supervision, writing – review and editing. U.S.: data curation, investigation, validation, writing – review and editing. B.F.: conceptualisation, methodology, supervision, funding acquisition, resources, writing.

Data availability statement. Two databases featuring all shown measurement data are published in the KITopen repository: https://doi.org/10.35097/qbs2jeamqbafebx8 (pressure data) and https://doi.org/10.35097/9xv5tk4tuk05d4mb (hot-wire data).

References

ANDERSON, W., BARROS, J.M., CHRISTENSEN, K.T. & AWASTHI, A. 2015 Numerical and experimental study of mechanisms responsible for turbulent secondary flows in boundary layer flows over spanwise heterogeneous roughness. *J. Fluid Mech.* **768**, 316–347.

ANDREOLLI, A., HUTCHINS, N., FROHNAPFEL, B. & GATTI, D. 2025 Temporal decay of secondary motions in turbulent channel flows. *J. Fluid Mech.* **1007**, A19.

ANDREOPOULOS, J. & WOOD, D.H. 1982 The response of a turbulent boundary layer to a short length of surface roughness. *J. Fluid Mech.* **118**, 143–164.

BOU-ZEID, E., ANDERSON, W., KATUL, G.G. & MAHRT, L. 2020 The persistent challenge of surface heterogeneity in boundary-layer meteorology: a review. *Boundary-Layer Meteorol.* **177**, 227–245.

CHUNG, D., HUTCHINS, N., SCHULTZ, M.P. & FLACK, K.A. 2021 Predicting the drag of rough surfaces. *Annu. Rev. Fluid Mech.* **53**, 439–471.

CHUNG, D., MONTY, J.P. & HUTCHINS, N. 2018 Similarity and structure of wall turbulence with lateral wall shear stress variations. *J. Fluid Mech.* **847**, 591–613.

DEAN, R.B. 1978 Reynolds number dependence of skin friction and other bulk flow variables in two-dimensional rectangular duct flow. *J. Fluids Engng* **100** (2), 215–223.

DEVENPORT, W.J. & LOWE, K.T. 2022 Equilibrium and non-equilibrium turbulent boundary layers. *Prog. Aerosp. Sci.* **131**, 376–421.

FROHNAPFEL, B., DEYN, L., VON, YANG, J., NEUHAUSER, J., STROH, A., ÖRLÜ, R. & GATTI, D. 2024 Flow resistance over heterogeneous roughness made of spanwise-alternating sandpaper strips. *J. Fluid Mech.* **980**, A31.

FROHNAPFEL, B., HASEGAWA, Y. & QUADRIO, M. 2012 Money versus time: evaluation of flow control in terms of energy consumption and convenience. *J. Fluid Mech.* **700**, 406–418.

GATTI, D., GÜTTLER, A., FROHNAPFEL, B. & TROPEA, C. 2015 Experimental assessment of spanwise-oscillating dielectric electroactive surfaces for turbulent drag reduction in an air channel flow. *Exp. Fluids* **56**, 110.

HANSON, R.E. & GANAPATHISUBRAMANI, B. 2016 Development of turbulent boundary layers past a step change in wall roughness. *J. Fluid Mech.* **795**, 494–523.

HINZE, J.O. 1973 Experimental investigation on secondary currents in the turbulent flow through a straight conduit. *Appl. Sci. Res.* **28**, 453–465.

HUTCHINS, N., GANAPATHISUBRAMANI, B., SCHULTZ, M.P. & PULLIN, D.I. 2023 Defining an equivalent homogeneous roughness length for turbulent boundary layers developing over patchy or heterogeneous surfaces. *Ocean Engng* **271**, 113454.

HUTCHINS, N., NICKELS, T., MARUSIC, I. & CHONG, M. 2009 Hot-wire spatial resolution issues in wall-bounded turbulence. *J. Fluid Mech.* **635**, 103–136.

JACOBI, I. & MCKEON, B.J. 2011 New perspectives on the impulsive roughness-perturbation of a turbulent boundary layer. *J. Fluid Mech.* **677**, 179–203.

JENSEN, R.M. & FOROOGHI, P. 2025 A study of turbulent flow over patchy roughness. *J. Fluid Mech.* **1006**, A28.

JIMÉNEZ, J. & PINELLI, A. 1999 The autonomous cycle of near-wall turbulence. *J. Fluid Mech.* **389**, 335–359.

LI, M., DE SILVA, C.M., ROUHI, A., BAIDYA, R., CHUNG, D., MARUSIC, I. & HUTCHINS, N. 2019 Recovery of wall-shear stress to equilibrium flow conditions after a rough-to-smooth step change in turbulent boundary layers. *J. Fluid Mech.* **872**, 472–491.

MODESTI, D., ENDRIKAT, S., HUTCHINS, N. & CHUNG, D. 2021 Dispersive stresses in turbulent flow over riblets. *J. Fluid Mech.* **917**, A55.

NEUHAUSER, J., SCHÄFER, K., GATTI, D. & FROHNAPFEL, B. 2022 Simulation of turbulent flow over roughness strips. *J. Fluid Mech.* **945**, A14.

NEUHAUSER, J., SCHMIDT, C., GATTI, D. & FROHNAPFEL, B. 2025 Predicting the global drag of turbulent channel flow over roughness strips. *Intl J. Heat Fluid Flow* **115**, 109848.

ÖRLÜ, R. & VINUESA, R. 2017 Thermal anemometry. In *Experimental Aerodynamics* (ed. S. Discetti & A. Ianiro), pp. 393–428. CRC Press Taylor & Francis.

PIROZZOLI, S., MODESTI, D., ORLANDI, P. & GRASSO, F. 2018 Turbulence and secondary motions in square duct flow. *J. Fluid Mech.* **840**, 631–655.

SCHLICHTING, H. 1979 *Boundary-Layer Theory*, 7th edn. McGraw Hill.

STROH, A., SCHÄFER, K., FOROOGHI, P. & FROHNAPFEL, B. 2020 Secondary flow and heat transfer in turbulent flow over streamwise ridges. *Intl J. Heat Fluid Flow* **81**, 108518.

VAN BUREN, T., FLORYAN, D., DING, L., HELLSTRÖM, L.H.O. & SMITS, A.J. 2020 Turbulent pipe flow response to a step change in surface roughness. *J. Fluid Mech.* **904**, A38.

VANDERWEL, C., STROH, A., KRIEGSEIS, J., FROHNAPFEL, B. & GANAPATHISUBRAMANI, B. 2019 The instantaneous structure of secondary flows in turbulent boundary layers. *J. Fluid Mech.* **862**, 845–870.

VINUESA, R., SCHLATTER, P. & NAGIB, H.M. 2015 On minimum aspect ratio for duct flow facilities and the role of side walls in generating secondary flows. *J. Turbul.* **16** (6), 588–606.

WANGSAWIJAYA, D.D., BAIDYA, R., CHUNG, D., MARUSIC, I. & HUTCHINS, N. 2020 The effect of spanwise wavelength of surface heterogeneity on turbulent secondary flows. *J. Fluid Mech.* **894**, A7.

WANGSAWIJAYA, D.D. & HUTCHINS, N. 2022 Investigation of unsteady secondary flows and large-scale turbulence in heterogeneous turbulent boundary layers. *J. Fluid Mech.* **934**, A40.

ZAMPIRON, A., CAMERON, S.M., STEWART, M.T., MARUSIC, I. & NIKORA, V.I. 2023 Flow development in rough-bed open channels: mean velocities, turbulence statistics, velocity spectra, and secondary currents. *J. Hydraul. Res.* **61** (1), 133–144.

ZHDANOV, O., JELLY, T.O. & BUSSE, A. 2024 Influence of ridge spacing, ridge width, and Reynolds number on secondary currents in turbulent channel flow over triangular ridges. *Flow Turbul. Combust.* **112**, 105–128.